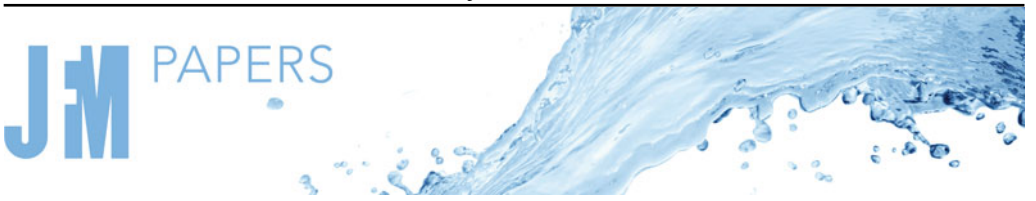
J. Fluid Mech. (2025), *vol.* 1024, A26, doi:10.1017/jfm.2025.10912



Analytical equations for mean wall-normal velocity and momentum integral in compressible boundary-layer flows

Tie Wei[1], **Zhaorui Li**[2], **Alessandro Ceci**[3] and **Sergio Pirozzoli**[3]

[1]Department of Mechanical Engineering, New Mexico Tech, Socorro, NM 87801, USA

[2]Department of Engineering, Texas A&M University-Corpus Christi, Corpus Christi, TX 78412, USA

[3]Dipartimento di Ingegneria Meccanica e Aerospaziale, Universitá di Roma 'La Sapienza', Via Eudossiana 18, Roma 00184, Italy

Corresponding author: Tie Wei, tie.wei@nmt.edu

(Received 24 July 2025; revised 31 October 2025; accepted 3 November 2025)

Analytical expressions for the mean wall-normal velocity and wall shear stress in compressible boundary layers are derived by integrating the mean continuity and momentum equations. In the constant-density limit, the momentum integral formulation recovers the classical Kármán–Pohlhausen equation for incompressible boundary-layer flows. In compressible regimes, particularly under strong pressure gradients, streamwise density gradients are shown to play a crucial role in shaping boundary-layer dynamics. The derived analytical equations are validated against high-fidelity direct numerical simulation data, demonstrating both accuracy and robustness. Furthermore, the analytical equations offer insights into the physical mechanisms of compressible boundary layers, particularly the influence of density gradients. The effect of compressibility on the wall-normal velocity is explicitly demonstrated, highlighting the distinct behaviour of compressible boundary layers compared with incompressible flows. Finally, an analytical expression for the skin-friction coefficient is developed, revealing its close connection to the mean wall-normal velocity at the boundary-layer edge.

Key words: compressible boundary layers, supersonic flow

1. Introduction

Integral analysis offers a powerful framework for deriving simplified, yet physically insightful, formulations that capture the essential characteristics of boundary-layer flows. In incompressible regimes, classical integral methods–originally developed by

© The Author(s), 2025. Published by Cambridge University Press.

https://doi.org/10.1017/jfm.2025.10912 Published online by Cambridge University Press

von Kármán (1921) and Pohlhausen (1921)–have been applied extensively to turbulent boundary layers and are now standard material in fluid mechanics textbooks.

Extending integral methods to compressible boundary layers introduces substantial complexity due to spatial variations in density, viscosity and temperature. Starting in the 1940s and 1950s, researchers began adapting these methods to compressible flow regimes (see reviews by Bertram 1968; Schlichting 1979). For instance, Schlichting (1979) presented integral forms of the momentum and energy equations for compressible laminar boundary layers. A widely used strategy involves applying compressibility transformations–such as those proposed by Crocco, Van Driest and Stewartson–to recast the governing equations into an incompressible-like form, thereby enabling the application of classical integral techniques (Bertram 1968).

More recently, Wenzel, Gibis & Kloker (2022) conducted an integral analysis of the mean momentum and total enthalpy equations to investigate the effects of compressibility, heat transfer and pressure gradients in turbulent boundary layers. Their study derived integral identities for the skin-friction and heat-transfer coefficients, providing quantitative insight into the cumulative influence of transport processes within the boundary layer.

Most existing integral analyses focus on the streamwise velocity, treating the mean wall-normal velocity only indirectly. In such formulations, the continuity equation is typically used to relate the wall-normal velocity to an integral of the streamwise velocity profile, without explicitly resolving its distribution. Recently, Wei and co-workers addressed this gap by deriving analytical expressions for the mean wall-normal velocity in incompressible turbulent boundary layers with and without pressure gradients (Wei, Li & Wang 2023*a*,*b*).

Building on this foundation, the present study extends the integral analysis framework to compressible turbulent boundary layers. Generalised integral relations are derived directly from the governing equations, without relying on compressibility transformations. Section 2 first presents an analytical expression for the mean wall-normal velocity at the boundary-layer edge, followed by its distribution across the wall-normal direction, and finally an expression for the mean wall shear stress. The analytical results are validated against direct numerical simulation data and further employed to gain physical insight into compressible boundary-layer flows. Section 3 summarises the main findings.

2. Integral analysis of compressible boundary-layer flows

Many terms in the analytical equations derived in this work can be accurately evaluated only using direct numerical simulation (DNS) data. Accordingly, the present formulations are validated against high-fidelity DNS results from Ceci *et al.* (2023), which investigate the interaction between an impinging shock wave and a turbulent boundary layer. The boundary layer is injected through the inflow plane at $x = 0$ and an oblique shock wave (β is the shock angle) is introduced by deflecting the flow by an angle θ, which nominally impinges on the boundary layer at $x_{imp} = 64\,\delta_0$, where δ_0 represents the boundary-layer thickness at the inflow. A mesh with $N_x \times N_y \times N_z = 1920 \times 240 \times 2016$ nodes is used for the DNS. The streamwise, wall-normal and spanwise domain sizes are set to $(L_x \times L_y \times L_z)/\delta_0 = 96 \times 20 \times 96$. An in-house solver, available as an open-source code (Bernardini *et al.* 2021; Salvadore *et al.* 2025), is used for all the DNS. Numerical boundary conditions at the far-field boundaries are managed according to a characteristic relaxation strategy (Pirozzoli & Colonius 2013). The recycling–rescaling procedure is used to generate the target flow at the inflow, as described by Ceci *et al.* (2022). The impinging shock is generated through local enforcement of the Rankine–Hugoniot jump relations at the top boundary, and periodic boundary conditions are applied to the spanwise boundaries.

https://doi.org/10.1017/jfm.2025.10912 Published online by Cambridge University Press

Case	M_∞	θ	Re_{θ_0}	Re_{δ_0}
G00_T08	2.28	8°	1200	15800

Table 1. Flow parameters for the DNS database of Ceci *et al.* (2023). Here M_∞ is the free stream Mach number, θ is the shock generator incidence angle; $Re_{\theta 0}$ and $Re_{\delta 0}$ represent the Reynolds numbers based on the momentum thickness and boundary-layer thickness at the inflow, respectively.

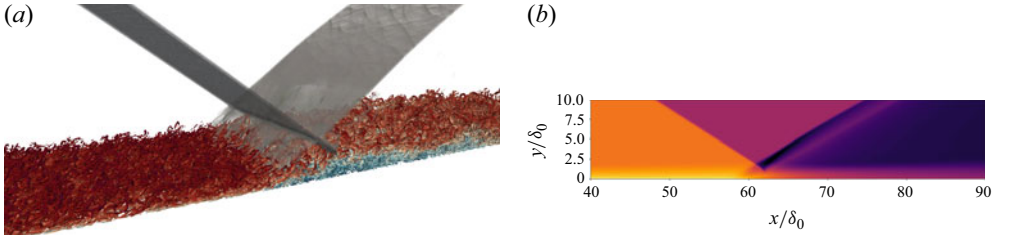


Figure 1. Flow structure in a supersonic shock/boundary-layer interaction using DNS data from Ceci *et al.* (2023): (*a*) instantaneous flow organisation highlighting coherent vortical structures and shock-induced separation, (*b*) time-averaged density field.

The wall is assumed to be isothermal, with temperature set to the nominal adiabatic value. The resulting simulations show good agreement with previous DNS by Pirozzoli & Bernardini (2011) and with experimental measurements by Piponniau *et al.* (2009), supporting the reliability of the set-up. A summary of the flow parameters is provided in table 1, while further details of the configuration are available in Ceci *et al.* (2023).

As shown in figure 1, the nominal shock impingement point in the DNS occurs at $x_{imp} = 64\delta_0$. Figure 2 presents the streamwise variation of several key quantities extracted from the DNS dataset, including the skin-friction coefficient, wall pressure, boundary-layer thickness (δ_{99}), mass displacement thickness (δ_1) and momentum thickness (δ_2). The boundary-layer thickness is defined using the 99 % criterion. The results demonstrate that δ_{99} varies smoothly outside the separation region but changes rapidly within it. Similarly, the mass displacement thickness and momentum thickness, integral measures of the boundary-layer profile, exhibit significant variation within the separation region.

2.1. *Mean wall-normal velocity at the boundary-layer edge*

For a statistically steady compressible turbulent boundary layer, the mean continuity equation is (see Huang, Coleman & Bradshaw 1995)

$$0 = \frac{\partial(\overline{\rho}\,\widetilde{u})}{\partial x} + \frac{\partial(\overline{\rho}\,\widetilde{v})}{\partial y}. \tag{2.1}$$

In this study, the Reynolds decomposition of a general flow variable φ is expressed as $\varphi = \overline{\varphi} + \varphi'$, where $\overline{\varphi}$ denotes the Reynolds-averaged value and φ' its fluctuation. The Favre (density-weighted) decomposition is written as $\varphi = \widetilde{\varphi} + \varphi''$, where $\widetilde{\varphi}$ is the Favre-averaged quantity and φ'' the corresponding fluctuation. In this notation, $\overline{\rho}$ is the Reynolds averaged density, and $\widetilde{u}$ and $\widetilde{v}$ are the Favre-averaged streamwise (x) and wall-normal (y) velocity components, respectively. Integrating the mean continuity (2.1) from the wall to the boundary-layer edge gives an expression for the Favre averaged mean wall-normal velocity at the boundary-layer edge as (see Appendix A for details)

https://doi.org/10.1017/jfm.2025.10912 Published online by Cambridge University Press

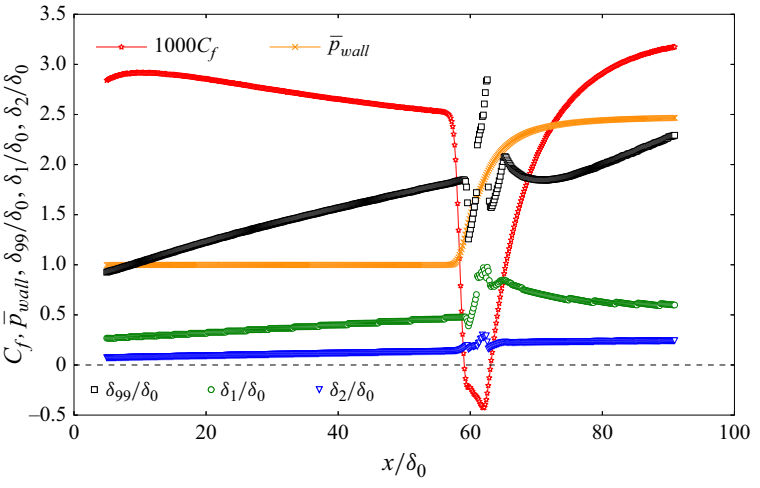


Figure 2. Friction coefficient C_f, mean wall pressure $\overline{p}_{wall}$, boundary-layer thickness, mass displacement thickness and momentum thickness variation in the streamwise direction in the DNS of shock/boundary-layer interaction by Ceci *et al.* (2023).

$$\frac{\widetilde{v}_e}{\widetilde{u}_e} = \frac{\mathrm{d}\delta_1}{\mathrm{d}x} - \frac{(\delta_e - \delta_1)}{\widetilde{u}_e}\frac{\mathrm{d}\widetilde{u}_e}{\mathrm{d}x} - \frac{(\delta_e - \delta_1)}{\overline{\rho}_e}\frac{\mathrm{d}\overline{\rho}_e}{\mathrm{d}x}, \tag{2.2}$$

where the subscript e indicates evaluation at the boundary-layer edge. For example, $\widetilde{u}_e$, $\widetilde{v}_e$ are the Favre-averaged streamwise and wall-normal velocity compoents at the boundary layer edge, respectively. δ_e is the boundary layer thickness, and $\overline{\rho}_e$ is the mean density at the boundary layer edge. Here, the mass displacement thickness for compressible boundary-layer flows is defined as $\delta_1 \overset{\text{def}}{=} \int_0^{\delta_e}(1 - ((\overline{\rho}\,\widetilde{u})/(\overline{\rho}_e\widetilde{u}_e)))\,\mathrm{d}y$ (Schlichting 1979). At the boundary-layer edge, terms $\overline{\rho' u'}$ and $\overline{\rho' v'}$ vanish, leading to $\widetilde{u}_e = \overline{u}_e + \overline{\rho' u'}_e/\overline{\rho}_e = \overline{u}_e$ and $\widetilde{v}_e = \overline{v}_e + \overline{\rho' v'}_e/\overline{\rho}_e = \overline{v}_e$. Consequently, (2.2) also applies to the Reynolds-averaged velocities.

Figure 3 compares the ratio $\widetilde{v}_e/\widetilde{u}_e$ obtained from simulations with the analytical prediction of (2.2). The agreement is excellent throughout most of the domain, with noticeable discrepancies only near the impingement point. In this region, sharp streamwise variations in δ_e and δ_1 (see figure 2) make accurate evaluation of the $\mathrm{d}/\mathrm{d}x$ terms particularly challenging in the postprocessing.

Figure 3 also shows that $\widetilde{v}_e$ remains much smaller than $\widetilde{u}_e$ (of the order of 0.5 %) away from the impingement point, specifically for $x/\delta_0 < 55$ or $x/\delta_0 > 80$ in the simulations of Ceci *et al.* (2023). In contrast, near the impingement point, the ratio $\widetilde{v}_e/\widetilde{u}_e$ increases sharply, reaching values of approximately -13 % at $x/\delta_0 \approx 64$. These larger values are omitted from the figure to maintain clarity in the regions away from the impingement point.

Compared with the incompressible analytical solution of Wei *et al.* (2023*a*), the key distinction in compressible flow is the last term in (2.2) that accounts for streamwise variations in $\overline{\rho}_e$. This density-gradient term is negligible far from the impingement point ($x/\delta_0 \lesssim 55$ or $x/\delta_0 \gtrsim 80$), where $\widetilde{v}_e/\widetilde{u}_e$ can be accurately approximated by $\mathrm{d}\delta_1/\mathrm{d}x$.

Upstream of the impingement point, the last two terms in (2.2) are negligibly small. Downstream of the impingement point, however, these terms become significant, and their

https://doi.org/10.1017/jfm.2025.10912 Published online by Cambridge University Press

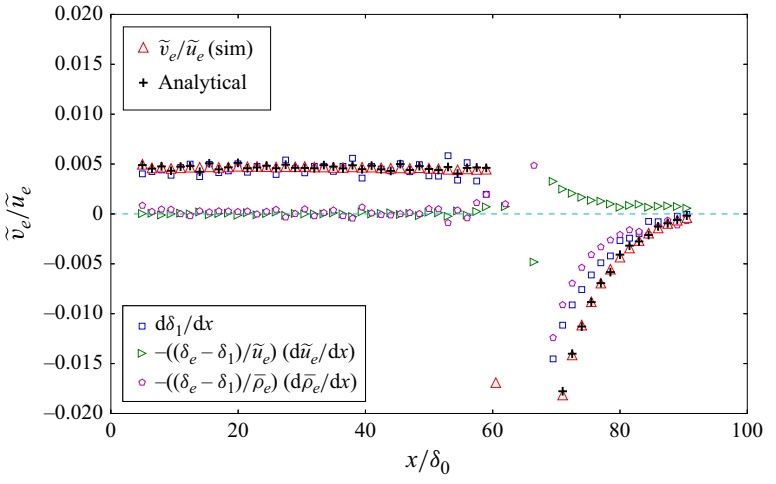


Figure 3. Comparison of the mean wall-normal velocity at the boundary-layer edge (red triangles) and analytical (2.2) (black plus symbols). The DNS data are from Ceci *et al.* (2023).

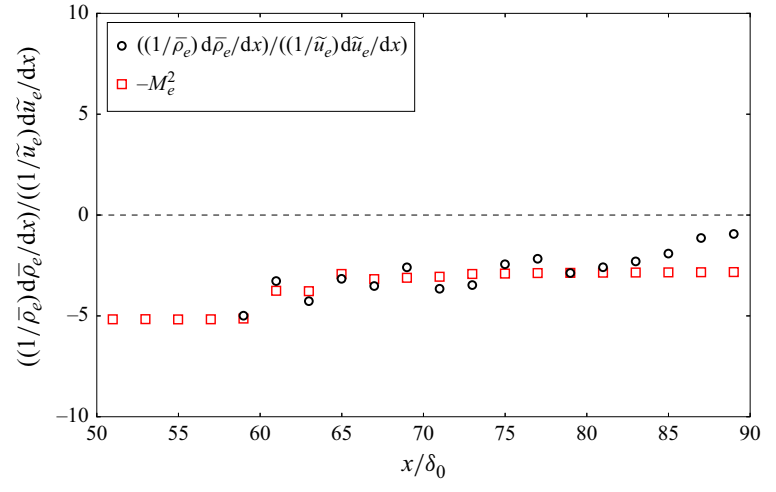


Figure 4. Ratio of the final two terms in (2.2), based on DNS data from Ceci *et al.* (2023).

profiles are closely correlated, as shown in figure 3. Their relationship can be quantified through the ratio, which, under the assumption of isentropic compressible flow, becomes

$$\frac{\dfrac{1}{\overline{\rho}_e}\dfrac{\mathrm{d}\overline{\rho}_e}{\mathrm{d}x}}{\dfrac{1}{\widetilde{u}_e}\dfrac{\mathrm{d}\widetilde{u}_e}{\mathrm{d}x}} \approx -M_e^2, \tag{2.3}$$

where M_e denotes the local Mach number at the boundary-layer edge (see Appendix B for details). This is checked in figure 4, where data upstream of the impingement point are omitted as both numerator and denominator are negligibly small (see figure 3). Downstream of the impingement point, we find that (2.3) applies with good accuracy.

From equations (2.3) and (2.2), the mean wall-normal velocity at the boundary-layer edge is directly related to the outer-flow Mach number. Specifically, we find that

https://doi.org/10.1017/jfm.2025.10912 Published online by Cambridge University Press

$$\frac{\widetilde{v}_e}{\widetilde{u}_e} \approx \frac{\mathrm{d}\delta_1}{\mathrm{d}x} - \frac{(\delta_e - \delta_1)}{\widetilde{u}_e}\frac{\mathrm{d}\widetilde{u}_e}{\mathrm{d}x}\left(1 - M_e^2\right). \tag{2.4}$$

In the incompressible limit, where the density is constant and $M_e \to 0$, (2.4) reduces to the mean wall-normal velocity relation for incompressible flows (Wei *et al.* 2023*a*). This confirms that (2.4) provides a unified description that consistently extends the incompressible theory to compressible supersonic boundary layers.

2.2. *Mean wall-normal velocity distribution*

To derive an analytical equation for the mean wall-normal velocity, we begin by transforming the mean continuity equation into a dimensionless form. This transformation is achieved by introducing the following normalised variables:

$$x^* \overset{\text{def}}{=} \frac{x}{L}, \qquad y^* \overset{\text{def}}{=} \frac{y}{\delta_e(x)}, \qquad U^*(x^*, y^*) \overset{\text{def}}{=} 1 - \frac{\overline{\rho}\,\widetilde{u}}{\overline{\rho}_e\widetilde{u}_e}, \qquad V^*(x^*, y^*) \overset{\text{def}}{=} \frac{\overline{\rho}\,\widetilde{v}}{\overline{\rho}_e\widetilde{v}_e}, \tag{2.5}$$

where L is a length scale in the x-direction and δ_e is the boundary-layer thickness. It is important to emphasise that the use of these normalised variables does not imply the presence or absence of self-similarity in the flow. Instead, it provides a mathematical framework that facilitates the derivation and analysis of the mean wall-normal velocity.

Using the defined normalised variables, the terms in the mean continuity (2.1) can be expressed as

$$\frac{\partial(\overline{\rho}\,\widetilde{u})}{\partial x} = \frac{\mathrm{d}\left(\overline{\rho}_e\widetilde{u}_e\right)}{\mathrm{d}x} - \frac{\mathrm{d}\left(\overline{\rho}_e\widetilde{u}_e\right)}{\mathrm{d}x}U^* + \frac{\overline{\rho}_e\widetilde{u}_e}{\delta_e}\frac{\mathrm{d}\delta_e}{\mathrm{d}x}y^*\frac{\partial U^*}{\partial y^*} - \frac{\overline{\rho}_e\widetilde{u}_e}{L}\frac{\partial U^*}{\partial x^*}, \tag{2.6}$$

$$\frac{\partial(\overline{\rho}\,\widetilde{v})}{\partial y} = \frac{\overline{\rho}_e\widetilde{v}_e}{\delta_e}\frac{\partial V^*}{\partial y^*}. \tag{2.7}$$

Simple mathematics produces a dimensionless continuity equation in the form of

$$\begin{aligned}\frac{\partial V^*}{\partial y^*} = &-\frac{\delta_e}{\overline{\rho}_e\widetilde{v}_e}\frac{\mathrm{d}\left(\overline{\rho}_e\widetilde{u}_e\right)}{\mathrm{d}x} + \left[\frac{1}{\widetilde{v}_e}\frac{\mathrm{d}\left(\widetilde{u}_e\delta_e\right)}{\mathrm{d}x} + \frac{\widetilde{u}_e\delta_e}{\widetilde{v}_e}\frac{1}{\overline{\rho}_e}\frac{\mathrm{d}\overline{\rho}_e}{\mathrm{d}x}\right]U^* \\ &- \frac{\widetilde{u}_e}{\widetilde{v}_e}\frac{\mathrm{d}\delta_e}{\mathrm{d}x}\frac{\partial(y^*U^*)}{\partial y^*} + \frac{\widetilde{u}_e}{\widetilde{v}_e}\frac{\delta_e}{L}\frac{\partial U^*}{\partial x^*}.\end{aligned} \tag{2.8}$$

Integrating (2.8) with respect to y^* yields an analytical equation for the mean wall-normal velocity distribution:

$$\begin{aligned}V^* = &\underbrace{-\left[\frac{\delta_e}{\widetilde{v}_e}\frac{\mathrm{d}\widetilde{u}_e}{\mathrm{d}x}\right]}_{a_I}y^* \underbrace{-\left[\frac{\widetilde{u}_e}{\widetilde{v}_e}\frac{\mathrm{d}\delta_e}{\mathrm{d}x}\right]}_{a_{II}}y^*U^* + \underbrace{\left[\frac{1}{\widetilde{v}_e}\frac{\mathrm{d}\left(\widetilde{u}_e\delta_e\right)}{\mathrm{d}x}\right]}_{-(a_I+a_{II})}\int_0^{y^*}U^*\mathrm{d}y^* \\ &+ \underbrace{\left[\frac{\widetilde{u}_e}{\widetilde{v}_e}\frac{\delta_e}{L}\right]}_{a_{III}}\int_0^{y^*}\frac{\partial U^*}{\partial x^*}\mathrm{d}y^* \underbrace{-\left[\frac{\widetilde{u}_e}{\widetilde{v}_e}\frac{\delta_e}{\overline{\rho}_e}\frac{\mathrm{d}\overline{\rho}_e}{\mathrm{d}x}\right]}_{a_{IV}}\int_0^{y^*}(1-U^*)\,\mathrm{d}y^*.\end{aligned} \tag{2.9}$$

Evaluation of (2.9) at $y^* = 1$ yields (2.2), providing the mean wall-normal velocity at the boundary-layer edge.

As an illustration, figure 5 compares the analytical solution from (2.9) with the simulated V^* profiles at two streamwise locations: one upstream of the impingement point and one near the impingement point. In both cases, the analytical prediction shows

https://doi.org/10.1017/jfm.2025.10912 Published online by Cambridge University Press

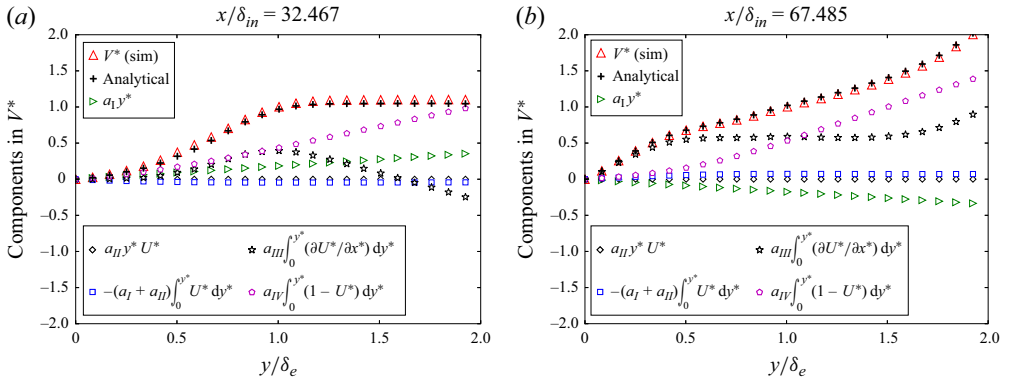


Figure 5. Comparison of the simulated mean wall-normal velocity profile with the analytical prediction from (2.9). Black plus symbols represent the sum of the five components in (2.9): (*a*) $x/\delta_0 = 32.467$, (*b*) $x/\delta_0 = 67.485$. The DNS data are from Ceci *et al.* (2023).

good agreement with the simulations, accurately capturing the mean wall-normal velocity distribution across the boundary layer.

The last term in (2.9) arises from density variations and is absent in incompressible flows. As shown in figure 5, this term plays a crucial role in shaping the mean wall-normal velocity distribution in compressible boundary layers. It can be further decomposed into two contributions: a linear growth component ($a_{IV} y^*$), and an integral component ($a_{IV}\int_0^{y^*} U^*\,\mathrm{d}y^*$). The latter approaches a constant value of $a_{IV}\delta_1/\delta_e$ at the boundary-layer edge. Consequently, (2.9) yields two distinct linear growth terms: the first term and the linear contribution from the density-gradient term. These linear behaviours are clearly visible in figure 5, particularly beyond the boundary-layer edge. Notably, the slope ratio of these two components, a_{IV}/a_I, matches that defined in (2.3). Since this ratio exceeds unity, the density-variation-induced contribution exhibits a steeper slope than the first term.

2.3. *Analytical equation for the wall shear stress*

The mean streamwise momentum equation for compressible boundary-layer flows is given by (Huang *et al.* 1995)

$$\frac{\partial(\overline{\rho}\,\widetilde{u}\,\widetilde{u})}{\partial x} + \frac{\partial(\overline{\rho}\,\widetilde{u}\,\widetilde{v})}{\partial y} = -\frac{\partial \overline{p}}{\partial x} + \frac{\partial \overline{\tau}_{xy}}{\partial y} - \frac{\partial(\overline{\rho}\widetilde{u''u''})}{\partial x} - \frac{\partial(\overline{\rho}\widetilde{u''v''})}{\partial y}, \tag{2.10}$$

where $\overline{p}$ is the mean pressure, $\overline{\rho}\,\widetilde{u''u''}$ and $\overline{\rho}\widetilde{u''v''}$ are the Favre-averaged Reynolds normal and shear stresses, respectively, and $\overline{\tau}_{xy}$ is the mean viscous shear stress. Integrating the momentum (2.10) from the wall to the boundary-layer edge and applying the corresponding boundary conditions yields

$$\int_0^{\delta_e} \frac{\partial(\overline{\rho}\,\widetilde{u}\,\widetilde{u})}{\partial x}\mathrm{d}y + \overline{\rho}_e\widetilde{u}_e\widetilde{v}_e = -\int_0^{\delta_e}\frac{\partial \overline{p}}{\partial x}\mathrm{d}y - \tau_{wall} - \int_0^{\delta_e}\frac{\partial(\overline{\rho}\,\widetilde{u''u''})}{\partial x}\mathrm{d}y. \tag{2.11}$$

Through a sequence of mathematical manipulations (see Appendix C), the momentum integral equation is derived:

https://doi.org/10.1017/jfm.2025.10912 Published online by Cambridge University Press

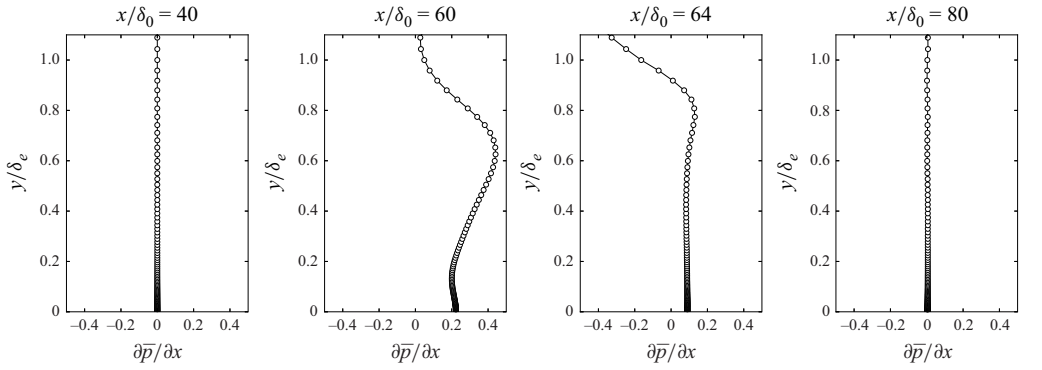


Figure 6. Wall-normal distributions of the streamwise pressure gradient $\partial\overline{p}/\partial x$ at four x-locations.

$$\tau_{wall} = \underbrace{\overline{\rho}_e\widetilde{u}_e\delta_1\frac{\mathrm{d}\widetilde{u}_e}{\mathrm{d}x}}_{\mathrm{I}} + \underbrace{\overline{\rho}_e\frac{\mathrm{d}\left(\widetilde{u}_e^2\delta_2\right)}{\mathrm{d}x}}_{\mathrm{II}} \underbrace{-\frac{\mathrm{d}}{\mathrm{d}x}\left(\int_0^{\delta_e}\left(\overline{\rho}\,\widetilde{u''u''}\right)\mathrm{d}y\right)}_{\mathrm{III}}$$
$$\underbrace{-\int_0^{\delta_e}\left(\frac{\partial\overline{p}}{\partial x}+\overline{\rho}_e\widetilde{u}_e\frac{\mathrm{d}\widetilde{u}_e}{\mathrm{d}x}\right)\mathrm{d}y}_{\mathrm{IV}} + \underbrace{\widetilde{u}_e^2\delta_2\frac{\mathrm{d}\overline{\rho}_e}{\mathrm{d}x}}_{\mathrm{V}}, \tag{2.12}$$

where $\delta_2 = \int_0^{\delta_e}(\overline{\rho}\widetilde{u})/(\overline{\rho}_e\widetilde{u}_e)(1-\widetilde{u}/\widetilde{u}_e)\,\mathrm{d}y$ is the momentum thickness defined for compressible flows (Schlichting 1979).

For incompressible flow, where the density is constant, the first two terms on the right-hand side of (2.12) reduce to the classical Kármán–Pohlhausen momentum integral equation (von Kármán 1921; Pohlhausen 1921; Gruschwitz 1931).

In studies of incompressible boundary layers with pressure gradients, Wei, Li & Wang (2024) demonstrated that the commonly assumed relation $\partial\overline{p}/\partial x = -\rho\overline{u}_e\,\mathrm{d}\overline{u}_e/\mathrm{d}x$ fails under strong pressure gradients, as $\partial\overline{p}/\partial x$ exhibits pronounced wall-normal variation. To account for this effect, Wei *et al.* (2023*a*) introduced an additional contribution (term IV) into the momentum integral formulation, thereby extending the classical Kármán–Pohlhausen formulation.

In compressible turbulent boundary layers, the streamwise pressure gradient $\partial\overline{p}/\partial x$ also exhibits pronounced wall-normal variation when the flow is subjected to strong pressure gradients, as shown in figure 6. The figure presents profiles of $\partial\overline{p}/\partial x$ at four streamwise locations. Away from the impingement region (e.g. $x/\delta_0 = 40$ and $x/\delta_0 = 80$), the pressure gradient remains nearly uniform in the wall-normal direction. In contrast, closer to the impingement point (e.g. $x/\delta_0 = 60$ and $x/\delta_0 = 64$), $\partial\overline{p}/\partial x$ shows significant wall-normal variation. The inclusion of term IV in (2.12) explicitly accounts for these wall-normal variations of $\partial\overline{p}/\partial x$, thereby improving the prediction of wall shear stress near the impingement point.

For compressible turbulent boundary layers, the general form of the momentum integral (2.12) introduces an additional term V, which arises from density variations, hence not present in the incompressible case (Wei *et al.* 2024). Note that the ratio of term V to term I in the momentum integral (2.12) is directly connected to the ratio given in (2.3), namely

https://doi.org/10.1017/jfm.2025.10912 Published online by Cambridge University Press

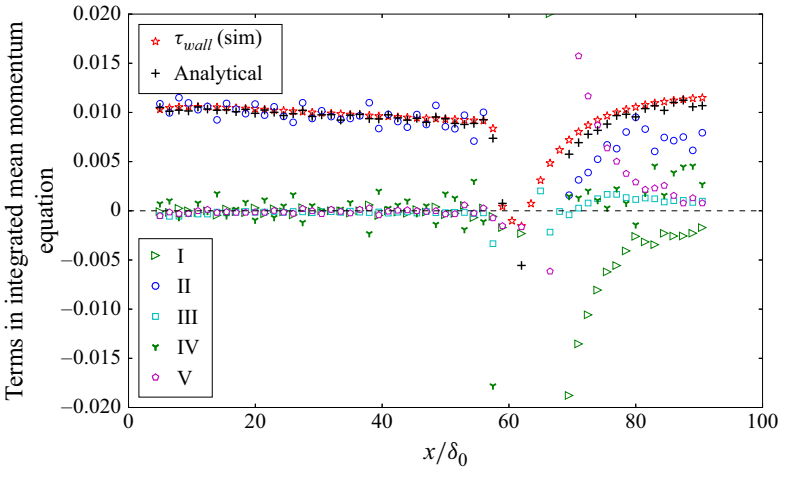


Figure 7. Comparison of the mean momentum integral (2.12) with DNS data from Ceci *et al.* (2023).

$$\frac{\widetilde{u}_e^2\delta_2\dfrac{\mathrm{d}\overline{\rho}_e}{\mathrm{d}x}}{\overline{\rho}_e\widetilde{u}_e\delta_1\dfrac{\mathrm{d}\widetilde{u}_e}{\mathrm{d}x}} = \frac{1}{H_{12}}\frac{\dfrac{1}{\overline{\rho}_e}\dfrac{\mathrm{d}\overline{\rho}_e}{\mathrm{d}x}}{\dfrac{1}{\widetilde{u}_e}\dfrac{\mathrm{d}\widetilde{u}_e}{\mathrm{d}x}}, \tag{2.13}$$

where $H_{12}=\delta_1/\delta_2$ is the shape factor. Figure 7 evaluates the momentum integral (2.12) using DNS data from Ceci *et al.* (2023). The analytical predictions, shown as black plus symbols, demonstrate excellent agreement with the DNS results. The scatter observed in the comparison arises primarily from numerical errors introduced during the numerical evaluation of the streamwise derivatives. Upstream of the impingement point ($x/\delta_0 \lesssim 55$), the second term on the right-hand side of (2.12) dominates the wall shear stress, while all other contributions remain negligible. In contrast, downstream of the impingement point, term I (associated with the pressure gradient) and term IV (arising from pressure-gradient variations in the wall-normal direction) become significant. Term V (arising from density gradient) in (2.12) plays a crucial role downstream of the impingement point, as illustrated in figure 7. In contrast, DNS data from Ceci *et al.* (2023) indicate that the contribution from the turbulent normal stress, $\overline{\rho}\,\widetilde{u''u''}$ (term III), remains small throughout the domain, including the region around the impingement point.

Schlichting (1979) presented a momentum integral equation for compressible laminar boundary-layer flows, assuming that pressure remains constant across the boundary layer. As a result, his formulation is limited to laminar flows subjected to zero or weak pressure gradients. In contrast, (2.12) is more general and applicable to both laminar and turbulent compressible boundary layers under arbitrary pressure-gradient conditions.

By substituting the analytical expression for $\widetilde{v}_e$ from (2.2) into the integral momentum (2.12), the latter can be recast into an alternative form, as detailed in the Appendix C:

$$\begin{aligned}\frac{\overline{\rho}_e\,\widetilde{u}_e\,\widetilde{v}_e}{\tau_{wall}} &= H_{12} + \frac{\overline{\rho}_e\,\widetilde{u}_e^2\,\delta_1}{\tau_{wall}}\,\frac{1}{H_{12}}\frac{\mathrm{d}H_{12}}{\mathrm{d}x} + \frac{H_{12}}{\tau_{wall}}\frac{\mathrm{d}}{\mathrm{d}x}\left(\int_0^{\delta_e}(\overline{\rho}\,\widetilde{u''u''})\,\mathrm{d}y\right)\\ &+ \frac{H_{12}}{\tau_{wall}}\int_0^{\delta_e}\left(\frac{\partial\overline{p}}{\partial x}+\overline{\rho}_e\widetilde{u}_e\frac{\mathrm{d}\widetilde{u}_e}{\mathrm{d}x}\right)\mathrm{d}y - \left(1+\frac{\delta_e}{\delta_1}+H_{12}\right)\frac{\overline{\rho}_e\,\widetilde{u}_e\,\delta_1}{\tau_{wall}}\,\frac{\mathrm{d}\widetilde{u}_e}{\mathrm{d}x} - \frac{\widetilde{u}_e^2\delta_e}{\tau_{wall}}\,\frac{\mathrm{d}\overline{\rho}_e}{\mathrm{d}x}.\end{aligned} \tag{2.14}$$

https://doi.org/10.1017/jfm.2025.10912 Published online by Cambridge University Press

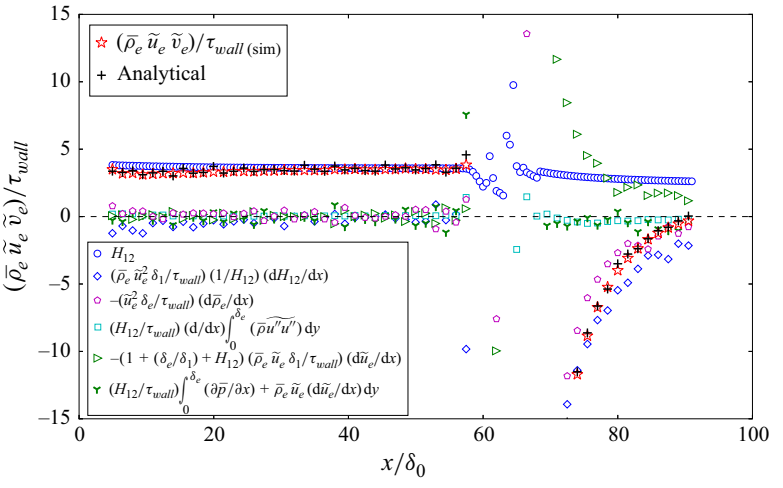


Figure 8. Comparison of the analytical expression for wall shear stress, (2.14), with DNS data from Ceci *et al.* (2023).

Figure 8 presents a comparison between the analytical (2.14) and the DNS data from Ceci *et al.* (2023). Overall, the analytical predictions show good agreement with the DNS results, demonstrating the accuracy of the derived equation.

For compressible boundary-layer flows subjected to weak pressure gradients, only the term H_{12} on the right side of (2.14) remains significant, while the contributions of the other terms become negligible. Consequently, for such flows, (2.14) simplifies to $(\overline{\rho}_e\,\widetilde{u}_e\,\widetilde{v}_e)/\tau_{wall} \approx H_{12}$, as illustrated in figure 8 for $x/\delta_0 < 55$. Note that the counterpart for incompressible zero-pressure-gradient turbulent boundary layer is $(\overline{u}_e\,\overline{v}_e)/u_\tau^2 \approx H_{12}$ (see Wei & Klewicki 2016, 2023).

By straightforward manipulation, (2.14) can be recast into a form suitable for evaluating the skin-friction coefficient, $C_f = \tau_{wall}/(0.5\,\overline{\rho}_e\,\widetilde{u}_e^2)$, as

$$C_f = \frac{2}{H_{12}}\left\{\frac{\widetilde{v}_e}{\widetilde{u}_e} - \frac{\delta_1}{H_{12}}\frac{\mathrm{d}H_{12}}{\mathrm{d}x} + \left(1+\frac{\delta_e}{\delta_1}+H_{12}\right)\frac{\delta_1}{\widetilde{u}_e}\frac{\mathrm{d}\widetilde{u}_e}{\mathrm{d}x}\right.$$
$$\left. - \frac{H_{12}}{\overline{\rho}_e\,\widetilde{u}_e^2}\left(\frac{\mathrm{d}}{\mathrm{d}x}\int_0^{\delta_e}(\widetilde{\overline{\rho}u''u''})\mathrm{d}y + \int_0^{\delta_e}\left(\frac{\partial\overline{p}}{\partial x}+\overline{\rho}_e\widetilde{u}_e\frac{\mathrm{d}\widetilde{u}_e}{\mathrm{d}x}\right)\mathrm{d}y\right) + \frac{\delta_e}{\overline{\rho}_e}\frac{\mathrm{d}\overline{\rho}_e}{\mathrm{d}x}\right\}. \tag{2.15}$$

This formulation expresses the skin-friction coefficient as a function of key boundary-layer parameters, including $\widetilde{u}_e$, $\widetilde{v}_e$, H_{12} and others, which evolve along the streamwise direction. Figure 9 compares the simulated friction coefficient C_f with the analytical prediction from (2.15) and its individual components, showing good overall agreement.

Under weak pressure-gradient conditions, C_f is governed primarily by the first term on the right-hand side of (2.15). Downstream of the impingement point, where the DNS results indicate flow separation, C_f becomes more strongly influenced by the terms involving $\widetilde{v}_e$ (first term on the right-hand side), $\mathrm{d}H_{12}/\mathrm{d}x$ (second term), the pressure gradient (third term) and the density gradient (last term). During and following boundary-layer separation, $\widetilde{v}_e$ (or the first term) becomes negative–indicating entrainment of free-stream fluid into the boundary layer. At the same time, H_{12} decreases rapidly in the streamwise direction, leading to a positive contribution from the second term.

https://doi.org/10.1017/jfm.2025.10912 Published online by Cambridge University Press

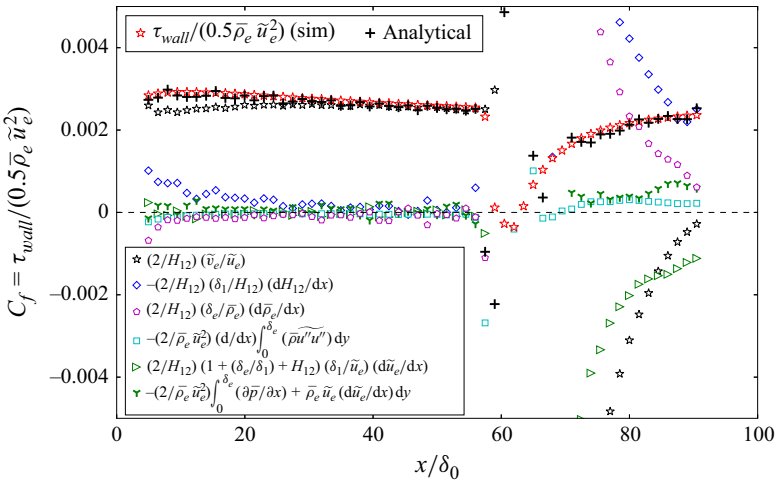


Figure 9. Comparison of the analytical expression for the friction coefficient, (2.15), with DNS data from Ceci *et al.* (2023).

In compressible boundary-layer flows, density variations (last term) also play a significant role in determining the skin-friction coefficient, particularly in regions of strong pressure gradients.

In free-shear turbulent flows, such as wakes and jets, the mean transverse velocity is much smaller than the mean axial velocity. Nevertheless, studies have demonstrated that it plays a key role in scaling turbulence quantities, including the turbulent shear stress (Wei & Livescu 2021; Wei, Livescu & Liu 2022). A similar situation arises in turbulent boundary-layer flows, where the mean wall-normal velocity is also much smaller than the streamwise velocity and is virtually impossible to measure directly in physical experiments. Consequently, the mean wall-normal velocity has often been overlooked in previous studies of boundary layers. Despite its small magnitude, the mean wall-normal velocity at the boundary-layer edge, $\widetilde{v}_e$, is closely related to the skin-friction coefficient, as shown in (2.15).

3. Summary

This study develops analytical expressions for the mean wall-normal velocity and a generalised Kármán–Pohlhausen momentum integral formulation that extends to compressible turbulent flows with arbitrary pressure gradients. In the limit of vanishing density variations, the incompressible relations are naturally recovered, demonstrating the generality of the formulation.

The derived analytical equations are validated against high-fidelity DNS data of shock-wave/boundary-layer interactions, demonstrating both accuracy and robustness. These formulations provide valuable tools for assessing and verifying numerical simulations of compressible flows.

Beyond validation, the analytical framework provides clear physical insight into how streamwise density gradients influence both the mean wall-normal velocity and the wall shear stress. The analysis explicitly demonstrates the impact of compressibility on the wall-normal velocity, emphasising the distinct dynamics of compressible turbulent boundary layers compared with their incompressible counterparts. The analytical equations further

https://doi.org/10.1017/jfm.2025.10912 Published online by Cambridge University Press

elucidate the relationship between the skin-friction coefficient and the mean wall-normal velocity in compressible turbulent boundary-layer flows.

Acknowledgements. We acknowledge that the results reported in this paper have been achieved with computational resources from EuroHPC JU Research Infrastructure resource Leonardo Booster based at CINECA, Casalecchio di Reno, Italy.

Funding. T.W. gratefully acknowledges support from the New Mexico Space Grant Consortium (NMSGC). Z.L. gratefully acknowledges support from the U.S. Department of Education under Award No. P116H240026. A.C. gratefully acknowledges financial support by Sapienza University of Rome under 'Add SAPI Excellence Fellowship 2024'.

Declaration of interests. The authors report no conflict of interest.

Appendix A. Derivation of wall-normal velocity

Integrating (2.1) from $y=0$ to $y=\delta_e$ results in

$$\begin{aligned}
0 &= \int_0^{\delta_e} \frac{\partial(\overline{\rho}\,\widetilde{u})}{\partial x}\mathrm{d}y + (\overline{\rho}\,\widetilde{v})\big|_0^{\delta_e} \\
&= \frac{\mathrm{d}}{\mathrm{d}x}\int_0^{\delta_e} (\overline{\rho}\,\widetilde{u})\mathrm{d}y - (\overline{\rho}_e\,\widetilde{u}_e)\frac{\mathrm{d}\delta_e}{\mathrm{d}x} + \overline{\rho}_e\,\widetilde{v}_e \\
&= \frac{\mathrm{d}}{\mathrm{d}x}\big(\overline{\rho}_e\,\widetilde{u}_e(\delta_e-\delta_1)\big) - \big(\overline{\rho}_e\,\widetilde{u}_e\big)\frac{\mathrm{d}\delta_e}{\mathrm{d}x} + \overline{\rho}_e\,\widetilde{v}_e, \\
&= \frac{\mathrm{d}}{\mathrm{d}x}\big(\overline{\rho}_e\,\widetilde{u}_e\delta_e\big) - \frac{\mathrm{d}}{\mathrm{d}x}\big(\overline{\rho}_e\,\widetilde{u}_e\delta_1\big) - \big(\overline{\rho}_e\,\widetilde{u}_e\big)\frac{\mathrm{d}\delta_e}{\mathrm{d}x} + \overline{\rho}_e\,\widetilde{v}_e, \\
&= \overline{\rho}_e\delta_e\frac{\mathrm{d}\widetilde{u}_e}{\mathrm{d}x} + \widetilde{u}_e\delta_e\frac{\mathrm{d}\overline{\rho}_e}{\mathrm{d}x} - \overline{\rho}_e\frac{\mathrm{d}\big(\widetilde{u}_e\delta_1\big)}{\mathrm{d}x} - \widetilde{u}_e\delta_1\frac{\mathrm{d}\overline{\rho}_e}{\mathrm{d}x} + \overline{\rho}_e\,\widetilde{v}_e,
\end{aligned} \tag{A1}$$

where the Leibniz integral rule has been applied to interchange the derivative and integral operations. Through straightforward algebraic manipulation, (2.2) can be derived for $\widetilde{v}_e$.

Appendix B. Ratio of $\mathrm{d}\overline{\rho}_e/\mathrm{d}x$ and $\mathrm{d}\widetilde{u}_e/\mathrm{d}x$

At the boundary-layer edge, the streamwise mean momentum equation reduces to

$$\overline{\rho}_e\widetilde{u}_e\frac{\mathrm{d}\widetilde{u}_e}{\mathrm{d}x} \approx -\frac{\mathrm{d}\overline{p}_e}{\mathrm{d}x}. \tag{B1}$$

Assuming that the flow at the boundary-layer edge can be approximated as isentropic, the relation $\overline{p}_e/\overline{\rho}_e^{\gamma} = \text{constant}$ holds, where $\gamma = C_p/C_v$ is the ratio of specific heats, with C_p and C_v denoting the specific heats at constant pressure and constant volume, respectively. Differentiating this expression with respect to x yields

$$\frac{\mathrm{d}\overline{p}_e}{\mathrm{d}x} = \gamma R\widetilde{T}_e\frac{\mathrm{d}\overline{\rho}_e}{\mathrm{d}x}, \tag{B2}$$

where R is the specific gas constant, and $\widetilde{T}_e$ is the temperature at the boundary-layer edge. Substituting (B2) into (B1) gives

$$\frac{\dfrac{1}{\overline{\rho}_e}\dfrac{\mathrm{d}\overline{\rho}_e}{\mathrm{d}x}}{\dfrac{1}{\widetilde{u}_e}\dfrac{\mathrm{d}\widetilde{u}_e}{\mathrm{d}x}} \approx -M_e^2 \tag{B3}$$

https://doi.org/10.1017/jfm.2025.10912 Published online by Cambridge University Press

where $M_e = \widetilde{u}_e/\sqrt{\gamma R \widetilde{T}_e}$ is the local Mach number at the boundary-layer edge. This expression establishes a relation between the density variations in supersonic boundary layers to the square of the edge Mach number (see Schlichting & Gersten 2016).

Appendix C. Derivation of momentum integral equation

The integral of the advective term $\partial(\overline{\rho}\,\widetilde{u}\,\widetilde{u})/\partial x$ can be rearranged as

$$\begin{aligned}
&\int_0^{\delta_e} \frac{\partial(\overline{\rho}\,\widetilde{u}\,\widetilde{u})}{\partial x}\mathrm{d}y \\
&= \frac{\mathrm{d}}{\mathrm{d}x}\int_0^{\delta_e}(\overline{\rho}\,\widetilde{u}\,\widetilde{u})\mathrm{d}y - \overline{\rho}_e\widetilde{u}_e^2\frac{\mathrm{d}\delta_e}{\mathrm{d}x} \\
&= \frac{\mathrm{d}}{\mathrm{d}x}\big((\overline{\rho}_e\widetilde{u}_e^2)(\delta_e-\delta_1-\delta_2)\big) - \overline{\rho}_e\widetilde{u}_e^2\frac{\mathrm{d}\delta_e}{\mathrm{d}x} \\
&= \delta_e\frac{\mathrm{d}(\overline{\rho}_e\widetilde{u}_e^2)}{\mathrm{d}x} - \frac{\mathrm{d}(\overline{\rho}_e\,\widetilde{u}_e^2\delta_1)}{\mathrm{d}x} - \frac{\mathrm{d}(\overline{\rho}_e\,\widetilde{u}_e^2\delta_2)}{\mathrm{d}x} \\
&= 2\overline{\rho}_e\widetilde{u}_e\delta_e\frac{\mathrm{d}\widetilde{u}_e}{\mathrm{d}x} + \widetilde{u}_e^2\delta_e\frac{\mathrm{d}\overline{\rho}_e}{\mathrm{d}x} - \widetilde{u}_e\delta_1\frac{\mathrm{d}(\overline{\rho}_e\widetilde{u}_e)}{\mathrm{d}x} - \overline{\rho}_e\widetilde{u}_e\frac{\mathrm{d}(\widetilde{u}_e\delta_1)}{\mathrm{d}x} - \frac{\mathrm{d}(\overline{\rho}_e\,\widetilde{u}_e^2\delta_2)}{\mathrm{d}x}. \qquad \text{(C1)}
\end{aligned}$$

Here, the definition of δ_2 and the Leibniz integral rule are applied to simplify the expression.

By applying the boundary condition and utilising (2.2) to express $\widetilde{v}_e$, the integral of the advective term $\partial(\overline{\rho}\,\widetilde{u}\,\widetilde{v})/\partial x$ becomes

$$\begin{aligned}
\overline{\rho}_e\widetilde{u}_e\widetilde{v}_e &= \overline{\rho}_e\widetilde{u}_e\left\{-\delta_e\frac{\mathrm{d}\widetilde{u}_e}{\mathrm{d}x} + \frac{\mathrm{d}(\widetilde{u}_e\delta_1)}{\mathrm{d}x} - \frac{(\delta_e-\delta_1)\widetilde{u}_e}{\overline{\rho}_e}\frac{\mathrm{d}\overline{\rho}_e}{\mathrm{d}x}\right\} \\
&= -\overline{\rho}_e\widetilde{u}_e\delta_e\frac{\mathrm{d}\widetilde{u}_e}{\mathrm{d}x} + \overline{\rho}_e\widetilde{u}_e\frac{\mathrm{d}(\widetilde{u}_e\delta_1)}{\mathrm{d}x} - \widetilde{u}_e^2\delta_e\frac{\mathrm{d}\overline{\rho}_e}{\mathrm{d}x} + \widetilde{u}_e^2\delta_1\frac{\mathrm{d}\overline{\rho}_e}{\mathrm{d}x}. \qquad \text{(C2)}
\end{aligned}$$

Combining (C1) and (C2) leads to the momentum integral (2.12).

To derive (2.14) for $\overline{\rho}_e\,\widetilde{u}_e\,\widetilde{v}_e/H_{12}$, we rewrite the term

$$\begin{aligned}
\frac{\mathrm{d}}{\mathrm{d}x}(\overline{\rho}_e\,\widetilde{u}_e^2\,\delta_2) &= \frac{\mathrm{d}}{\mathrm{d}x}\left(\frac{\overline{\rho}_e\,\widetilde{u}_e^2\,\delta_1}{H_{12}}\right) \\
&= \frac{H_{12}\dfrac{\mathrm{d}(\overline{\rho}_e\,\widetilde{u}_e^2\,\delta_1)}{\mathrm{d}x} - \overline{\rho}_e\,\widetilde{u}_e^2\,\delta_1\dfrac{\mathrm{d}H_{12}}{\mathrm{d}x}}{H_{12}^2} \\
&= \frac{\overline{\rho}_e\,\widetilde{u}_e\,\widetilde{v}_e}{H_{12}} + \frac{\widetilde{u}_e(\delta_e+\delta_1)}{H_{12}}\frac{\mathrm{d}(\overline{\rho}_e\widetilde{u}_e)}{\mathrm{d}x} - \frac{\widetilde{u}_e^2\delta_1}{H_{12}}\frac{\mathrm{d}\overline{\rho}_e}{\mathrm{d}x} - \frac{\overline{\rho}_e\widetilde{u}_e^2\delta_1}{H_{12}^2}\frac{\mathrm{d}H_{12}}{\mathrm{d}x}. \qquad \text{(C3)}
\end{aligned}$$

The remaining steps in the derivation follow straightforwardly.

https://doi.org/10.1017/jfm.2025.10912 Published online by Cambridge University Press

References

Bernardini, M., Modesti, D., Salvadore, F. & Pirozzoli, S. 2021 STREAmS: a high-fidelity accelerated solver for direct numerical simulation of compressible turbulent flows. *Comput. Phys. Commun.* **263**, 107906.

Bertram, M.H. 1968 Compressible turbulent boundary layers. *Tech. Rep.*. NASA SP-216.

Ceci, A., Palumbo, A., Larsson, J. & Pirozzoli, S. 2022 Numerical tripping of high-speed turbulent boundary layers. *Theor. Comput. Fluid Dyn.* **36** (6), 865–886.

Ceci, A., Palumbo, A., Larsson, J. & Pirozzoli, S. 2023 On low-frequency unsteadiness in swept shock wave–boundary layer interactions. *J. Fluid Mech.* **956** (R1), 1–11.

Gruschwitz, E. 1931 *Die Turbulente Reibungsschicht in Ebener Strömung Bei Druckabfall Und Druckanstiegs*. Springer.

Huang, P.G., Coleman, G.N. & Bradshaw, P. 1995 Compressible turbulent channel flows: DNS results and modelling. *J. Fluid Mech.* **305**, 185–218.

von Kármán, T.V. 1921 Über laminare und turbulente Reibung. *ZAMM - J. Appl. Maths Mech. / Z. Angew. Math. Mech.* **1** (4), 233–252.

Piponniau, S., Dussauge, J.-P., Debieve, J.-F. & Dupont, P. 2009 A simple model for low-frequency unsteadiness in shock-induced separation. *J. Fluid Mech.* **629**, 87–108.

Pirozzoli, S. & Bernardini, M. 2011 Direct numerical simulation database for impinging shock wave/turbulent boundary-layer interaction. *AIAA J.* **49** (6), 1307–1312.

Pirozzoli, S. & Colonius, T. 2013 Generalized characteristic relaxation boundary conditions for unsteady compressible flow simulations. *J. Comput. Phys.* **248**, 109–126.

Pohlhausen, K. 1921 Zur näherungsweisen integration der differentialgleichung der iaminaren grenzschicht. *ZAMM-J. Appl. Maths Mech. / Z. Angew. Math. Mech.* **1** (4), 252–290.

Salvadore, F. *et al.* 2025 STREAmS-2.1: Supersonic turbulent accelerated Navier–Stokes solver version 2.1. *Comput. Phys. Commun.* **314** (1), 109652.

Schlichting, H. 1979 *Boundary-Layer Theory*. McGraw-Hill, Inc.

Schlichting, H. & Gersten, K. 2016 *Boundary-Layer Theory*. Springer.

Wei, T. & Klewicki, J. 2016 Scaling properties of the mean wall-normal velocity in zero-pressure-gradient boundary layers. *Phys. Rev. Fluids* **1** (8), 082401.

Wei, T. & Klewicki, J. 2023 Integral relation in zero-pressure-gradient boundary layer flows. *Phys. Rev. Fluids* **8** (124601), 1–10.

Wei, T., Li, Z., Knopp, T. & Vinuesa, R. 2023*a* The mean wall-normal velocity in turbulent-boundary-layer flows under pressure gradient. *J. Fluid Mech.* **975** (A27), 1–20.

Wei, T., Li, Z. & Wang, Y. 2023*b* New formulations for the mean wall-normal velocity and Reynolds shear stress in a turbulent boundary layer under zero pressure gradient. *J. Fluid Mech.* **969** (A3), 1–15.

Wei, T., Li, Z. & Wang, Y. 2024 New momentum integral equation applicable to boundary layer flows under arbitrary pressure gradients. *J. Fluid Mech.* **984**, A64.

Wei, T. & Livescu, D. 2021 Scaling of the mean transverse flow and Reynolds shear stress in turbulent plane jet. *Phys. Fluids* **33** (3), 035142.

Wei, T., Livescu, D. & Liu, X. 2022 Scaling patch analysis of planar turbulent wake. *Phys. Fluids* **34** (065116), 1–7.

Wenzel, C., Gibis, T. & Kloker, M. 2022 About the influences of compressibility, heat transfer and pressure gradients in compressible turbulent boundary layers. *J. Fluid Mech.* **930**, A1.

https://doi.org/10.1017/jfm.2025.10912 Published online by Cambridge University Press